


ORIGINAL ARTICLE

Relationship between aqueous chemistry and composition, structure, and solubility of sodium aluminosilicate hydrates

Trevor Williamson¹ | Lynn E. Katz¹ | Joonkyoung Han¹ | Howard A. Dobbs² | Bradley F. Chmelka² | Gaurav Sant³ | Maria C. G. Juenger¹ 

¹Department of Civil, Architectural and Environmental Engineering, University of Texas at Austin, Austin, TX, USA

²Department of Chemical Engineering, University of California, Santa Barbara, Santa Barbara, CA, USA

³Departments of Civil and Environmental Engineering and Materials Science and Engineering, California Nanosystems Institute, University of California, Los Angeles, Los Angeles, CA, USA

Correspondence

Maria C. G. Juenger, Department of Civil, Architectural and Environmental Engineering, University of Texas at Austin, 301 E. Dean Keeton St. C1700, Austin, TX 78712, USA.

Email: mjuenger@mail.utexas.edu

Funding information

Federal Highway Administration, Grant/Award Number: DTFH61-13-H-00011

Abstract

Inorganic polymer binders (IPBs) are synthesized by the activation of aluminosilicate precursors with an alkaline solution such as sodium hydroxide. This paper studies the relationship between the composition, structure, and solubility of sodium aluminosilicate hydrates (N–A–S–(H)), the primary binding phase in IPBs. It was found that changing the aqueous Si/Al ratio had little effect on N–A–S–(H) Si/Al ratio, but small changes in the aqueous Si/Na ratio led to substantial changes in N–A–S–(H) Si/Al ratio. Early N–A–S–(H) products were found to be X-ray amorphous, but a rapid transition to the crystalline phase faujasite occurred after several weeks of aging. The transition of the solid amorphous phase to faujasite was accompanied by a rapid drop in aqueous Si(IV) and Al(III) concentrations. Solubility products were determined, temporally, for the N–A–S–(H) before and after the transition to faujasite and represent new contributions to the literature, particularly for the amorphous state. The results presented here provide fundamental insights that are needed for the development of kinetic and thermodynamic models that can establish phase balances and evolutions of IPBs across a range of precursor compositions and synthesis conditions.

KEYWORDS

alkali activation, aluminosilicates, amorphous, solubility, zeolites

1 | INTRODUCTION

Inorganic polymer binders (IPBs), also known as geopolymers, are a relatively new class of infrastructure materials that have recently received substantial attention in the scientific literature owing to their potential to serve as an alternative to ordinary portland cement (OPC).^{1–3} These binders are synthesized by the chemical activation of an aluminosilicate powder by a highly alkaline aqueous solution, most commonly sodium or potassium hydroxide, to form primarily an amorphous sodium aluminosilicate phase referred to as N–A–S–(H). Bulk Si/Al, Na/Al, and H₂O/Na ratios, as well as activator Si/Na ratios, are considered the most important

compositional parameters, and activating solutions with pre-dissolved silica are often used to achieve target compositions.^{4–6} Fly ash, a coal combustion product used extensively as a partial replacement for OPC in concrete, is one of the most promising aluminosilicate sources for IPBs since it is available on a large scale at relatively low cost with the added motivation of diverting fly ash from landfills. Fly ash-based IPBs (often referred to in the literature as alkali-activated fly ash [AAFA]) are the primary focus of the research presented here, although much of the discussion is relevant to IPBs based on other aluminosilicate sources (eg, metakaolin).

An extensive body of research has demonstrated comparable mechanical properties (compressive strength,

stiffness)^{4,7-9} as well as superior dimensional stability^{10,11} and durability (resistance to corrosion, alkali-silica reaction, acid attack)¹²⁻¹⁶ of IPB concrete compared to OPC concrete. Much of the existing research, however, has focused on the characterization and evaluation of a variety of aluminosilicate sources with significant levels of variation (in both composition and solubility) from one source to the next and inhomogeneity within a given source. While the understanding of basic mechanisms that govern product formation, microstructure development and, ultimately, engineering properties has advanced significantly, substantial progress in the understanding of the reaction thermodynamics is still required.¹⁷ For example, while several studies have examined the phases formed, documented in a review by Provis et al.,¹⁷ very few studies have quantified solubility products needed as thermodynamic modeling inputs for these phases,¹⁸ particularly with respect to the primary reaction product, an amorphous N-A-S-(H) phase. As a result, it is not possible to a priori optimize conditions for the formation of particular phases or to assess their long-term stability.

The general process of alkali-activation of aluminosilicate solids is shown schematically in Figure 1. The process begins with rapid dissolution of the initial solid particles (Figure 1A) through alkaline hydrolysis, leading to a highly concentrated aqueous solution containing sodium, $\text{Al}(\text{OH})_4^-$ (the dominant aqueous aluminum hydroxide species under alkaline conditions), and various silicate species depending on the pH of solution and Si/Na ratio (Figure 1B). As the solution becomes saturated with respect to binding phases, the hydrolyzed silicate and aluminate species polymerize, condense, and precipitate (Figure 1C). Previous literature has paid much attention to macroscopic factors impacting dissolution of various silicate and aluminate-bearing phases from fly ash and to the effect of bulk Si/Al ratio of the system on engineering properties.¹⁹⁻²¹ The formation and fundamental physical/chemical properties of the solid binding phase that forms from a liquid phase of given composition has been explored briefly,

however, and is critical in developing a full understanding of the factors influencing engineering properties.⁸ Linking bulk Si/Al ratio directly to engineering properties is often futile because of the difficulties in deconvoluting the effects of the many variables discussed hitherto. The study described here addressed that challenge by mixing solutions containing fully dissolved reagent grade silicates and aluminates, eliminating the complex variables that lead to a given aqueous phase composition, which occur during dissolution and subsequent reactions. This approach allows for complete stoichiometric control over the solution composition to elucidate directly the development of N-A-S-(H) structure and composition as it relates to a given solution composition.

The research presented here investigated the relationship between pore solution composition and the solid's composition, structure, and solubility to better understand the formation of OPC-free IPBs. To this end, N-A-S-(H) was synthesized from reagent grade precursors across a range of compositions, allowing stoichiometric control of the reactants. N-A-S-(H) compositions were determined by mass balance and thermogravimetric analysis (TGA). Nuclear magnetic resonance (NMR) spectroscopy and X-ray diffraction (XRD) were applied to probe the atomic structure of N-A-S-(H) as a function of solution composition. Additionally, solubility products (K_{sp}) of N-A-S-(H) were determined by monitoring the ionic concentration of the supernatant solution over time using inductively coupled plasma optical emission spectroscopy (ICP-OES). The resulting understanding of product composition and structure will be useful in predicting the performance of IPBs made from commercial fly ashes across a range of compositions, while solubility data are critical to the development of thermodynamic models describing IPB product development. This work is also relevant to the formation of aluminosilicate in alkaline environments in general, especially formation of zeolite, which is an area of interest for catalysis and other technological applications, as the structure of the resultant aluminosilicate drives the material properties.

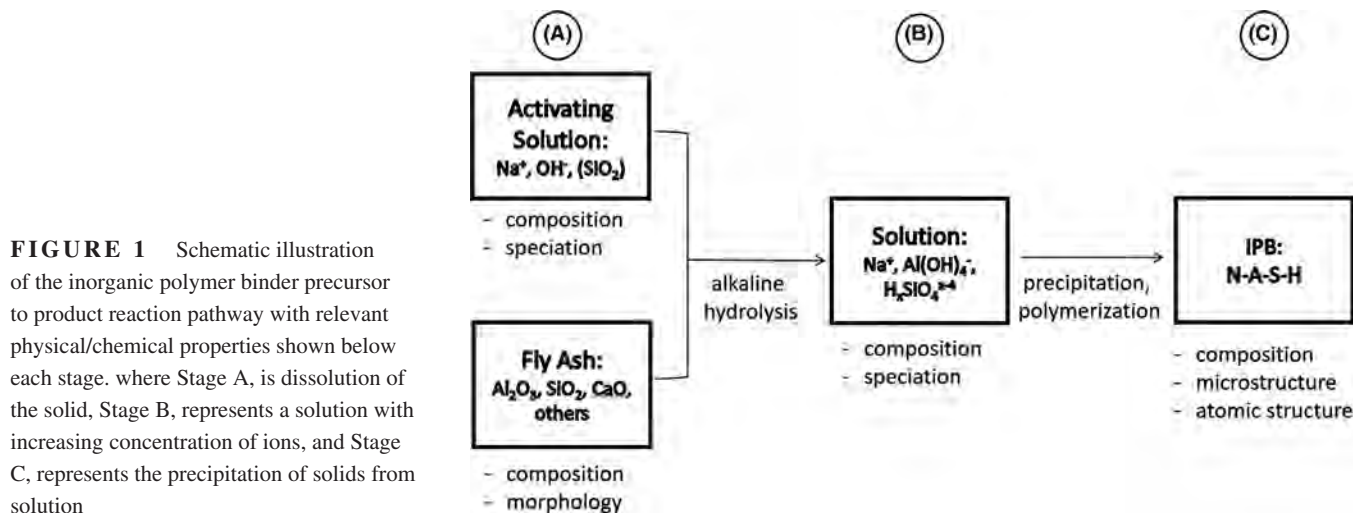


FIGURE 1 Schematic illustration of the inorganic polymer binder precursor to product reaction pathway with relevant physical/chemical properties shown below each stage. where Stage A, is dissolution of the solid, Stage B, represents a solution with increasing concentration of ions, and Stage C, represents the precipitation of solids from solution

2 | EXPERIMENTAL MATERIALS AND METHODS

2.1 | N–A–S–(H) synthesis

N–A–S–(H) samples were synthesized in batch reactors by mixing appropriate proportions of de-gassed (by boiling for 10 minutes) Milli-Q water (Merk Millipore) with sodium silicate and sodium aluminate solutions in a N₂-filled glove box to achieve bulk molar Si/Al ratios of 1, 1.5, and 2 following the methods detailed by Williamson et al.²² The Si/Al ratios were chosen based on the studies in the literature that have reported optimum molar Si/Al ratios in the range of 1 to 2.^{4,9,23,24} The sodium silicate-activating solution had a Si/Na molar ratio of 0.1. This ratio was intentionally selected to be low enough so that the dissolved silicate species in this solution would be monomeric.²⁵

A separate set of samples was prepared with the silicate stock solution Si/Na molar ratio varying from 0.1 to 1.0 and bulk Si/Al varying from 0.89 to 9.58 to investigate the effect of silicate-activating solution on N–A–S–(H) composition. In these experiments, Si/Na was manipulated by increasing the silicic acid concentration in the silicate stock solution so that the final sodium hydroxide concentration in all samples remained constant (and the same as in the experiments with constant silicate solution Si/Na ratio) at 1 M. The same sodium aluminate stock solution (0.1 M sodium aluminate) was used in these experiments as in the previous experiments.

All samples were reacted for 56 days at 50°C in 40 mL polyethylene tubes, rotated continuously at 8 rpm. This reaction temperature falls within the range of curing temperatures found in the literature for IPBs.^{16,26–28} Supernatant Si(IV) and Al(III) concentrations were monitored over time, and only small changes (<10%) in concentrations were observed after 56 days. For the bulk molar Si/Al = 1 and Si/Al = 2 N–A–S–(H) samples, aliquots of the supernatant (following the procedure outlined in the next section) were analyzed for total Si and Al concentrations at 3, 7, 10, 14, 29, and 56 days. For the bulk molar Si/Al = 1.5 N–A–S–(H) samples, aliquots were analyzed for total Si and Al concentrations at 7, 14, 29, 42, and 56 days. For each concentration, multiple samples were prepared so that a fresh sample (with no aliquot removed previously) could be analyzed at the final measurement time of 56 days, which are the samples used to calculate solubility products.

2.2 | Aqueous and solid-state characterization

Aliquots from supernatants of reacted samples were filtered using a 0.2 µm polyvinylidene fluoride syringe filter and diluted with 3% (v/v) nitric acid. Supernatant Na, Si,

and Al concentrations were determined using a Varian 10-ES ICP-OES with a SPS 3 autosampler and *ICP Expert II* software (v 1.1). All ICP measurements were taken in triplicate, and each concentration value reported represents the average of three measurements. The solution concentrations along with solid compositions (calculated by mass balance using solution concentrations combined with TGA data) were used to calculate temperature-dependent solubility products using PHREEQC software (version OS X). Reactions and constants used for modeling were taken from the LLNL database as shown in the Supporting Information.

Solids were either centrifuged and freeze-dried for XRD, solid-state NMR, and ICP-OES analysis, or vacuum-filtered for TGA. The centrifuged solids were triple-rinsed with Milli-Q water by dispersing them in the water, centrifuging at 3000 g for 10 minutes, and decanting. They were then frozen with liquid N₂ for 5 minutes, freeze-dried at –50°C and 5 Pa for 48 hours using a Labconco Freezone Bulk Tray Dryer and stored at –20°C under N₂ until further analysis. The vacuum-filtered solids were filtered using nylon filter membranes with a pore size of 0.45 µm and a diameter of 47 mm. The solids were washed and then stored under N₂ at 4°C until undergoing TGA.

Powder XRD was performed on a Rigaku MiniFlex operated at 40 kV and 15 mA using CuKα radiation. The powder samples were scanned from 5° to 60° 2θ at a rate of 2° 2θ/minute and a step size of 0.02° 2θ. Solid-state NMR was performed on a Bruker AVANCE-II NMR spectrometer, with an 11.7 T wide-bore superconducting magnet, operating at frequencies of 500.24 MHz for ¹H, 99.38 MHz for ²⁹Si, and 130.35 MHz for ²⁷Al. The ²⁹Si NMR spectra were recorded at 273 K with a MAS frequency of 10 kHz at 11.3 T. A D₁ of 200 seconds was used for the early time points, while the 28-day spectra were acquired with a D₁ of 60 seconds, which accounted for full relaxation of the signals. The ²⁷Al NMR spectra were recorded at 273 K with a MAS frequency of 10 kHz at 11.3 T. A D₁ of 0.5 second was sufficient for full relaxation of the signals. Thermogravimetric data were collected using a Mettler Thermogravimetric Analyzer, Model TGA/DSC 1 with a sensitivity of 2 µg. The vacuum-filtered samples were equilibrated at 40°C for 1 hour and then heated from 40°C to 600°C under N₂ at a flow rate of 20 mL/minute with a heating rate of 20°C/minute in pure aluminum oxide crucibles. The 40°C equilibration period was to allow for the evaporation of excess water so that the water content contained in the solid phases could be accurately quantified.

Some of the freeze-dried solids were digested using a mixture of hydrofluoric and hydrochloric acids and analyzed by ICP-OES to determine the solid composition. The solids were digested following a detailed protocol developed by Inorganic Ventures specifically for the compositional analysis of zeolites. The protocol uses two premixed, proprietary

solutions: (a) Inorganic Ventures UA-1, comprised of proprietary proportions hydrofluoric and hydrochloric acids to digest the solids and (b) Inorganic Ventures UNS-1, comprised of proprietary proportions of triethanolamine and triethylenetetramine to buffer the acids used for digestion. To perform the digestion, 80 to 100 mg of freeze-dried solids were weighed to the nearest 0.1 mg and added to a polyethylene bottle. Ten drops of deionized water were then added to the solids, and the bottle was swirled to hydrate the surface of the solids. Next, 10 mL of UA-1 and 0.5 mL of concentrated nitric acid (trace metal grade, Fisher) were added and the vessel was capped and shaken for 3 minutes (at this point, the solid appeared completely dissolved to the naked eye). The resulting solution was neutralized by adding 50 mL of UNS-1, and the final solution weight was adjusted to 500 g using deionized water. Finally, the solution was analyzed using ICP-OES in the same way that supernatant concentrations were measured (described previously).

3 | RESULTS AND DISCUSSION

3.1 | Evolution of aqueous chemistry and solid structure

Changes in solution Si and Al concentrations over time were monitored in order to establish the time required for N–A–S–(H) solids to reach equilibrium. Changes in Si and Al were chosen over changes in Na concentrations, because the relatively high concentrations of Na (>1 M) in all systems meant that the relative change in solution phase Na was small compared to the total Na in the system. As a result, the absolute error would have been higher compared to the measured values.

Figures 2–4 show changes in Si and Al concentrations over time for N–A–S–(H) reacted at 50°C with bulk Si/Al = 1.0, 1.5, and 2.0, respectively. Initially, both Si and Al concentrations decreased rapidly at all three compositions, corresponding to rapid precipitation of N–A–S–(H) solids. Indeed, precipitated solids were observed visually in all experiments within seconds of combining the sodium aluminate and sodium silicate stock solutions.

Concentrations of Si and Al became relatively stable in N–A–S–(H) with bulk Si/Al = 1.0 (Figure 2) after about 14 days (there was only a 5.4% decrease in Si and 5.8% decrease in Al between 14 and 29 days). At Si/Al = 2.0 (Figure 4) significant changes in concentrations were observed between 14 and 29 days (17% decrease in Si and 82% decrease in Al). At Si/Al = 1.5 (Figure 3); there were 30% and 84% decrease in Si and Al, respectively, between 14 and 29-day measurements, after which Si and Al concentrations remained relatively stable until the 56-day measurements. In all three systems, measurable changes in concentrations were observed until the 56-day measurements, at which point the

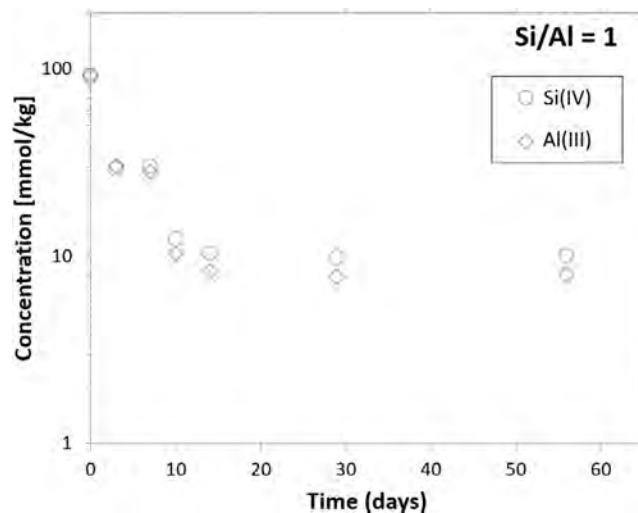


FIGURE 2 Changes in supernatant Si and Al concentrations over time for N–A–S–(H) reacted at 50°C with bulk Si/Al = 1.0. The error from triplicate measurements is smaller than the size of the symbol, so error bars are not shown [Color figure can be viewed at wileyonlinelibrary.com]

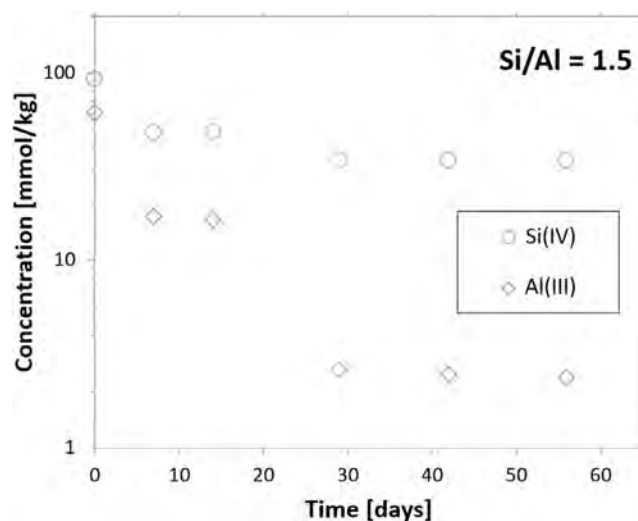


FIGURE 3 Changes in supernatant Si and Al concentrations over time for N–A–S–(H) reacted at 50°C with bulk Si/Al = 1.5. The error from triplicate measurements is smaller than the size of the symbol, so error bars are not shown [Color figure can be viewed at wileyonlinelibrary.com]

reacted solids and solutions were analyzed to determine solid composition and structure, solution composition, and solubility products.

Interestingly, the presence of an early “plateau” in Si and Al concentrations can be observed in all three experiments, where concentrations leveled off as if approaching equilibrium, but then rapidly decreased again. For the Si/Al = 2.0 experiment, this plateau started at about 3 days and continued until the 14-day measurements. A much shorter plateau was observable at Si/Al = 1.0, occurring between the 3 and 7-day

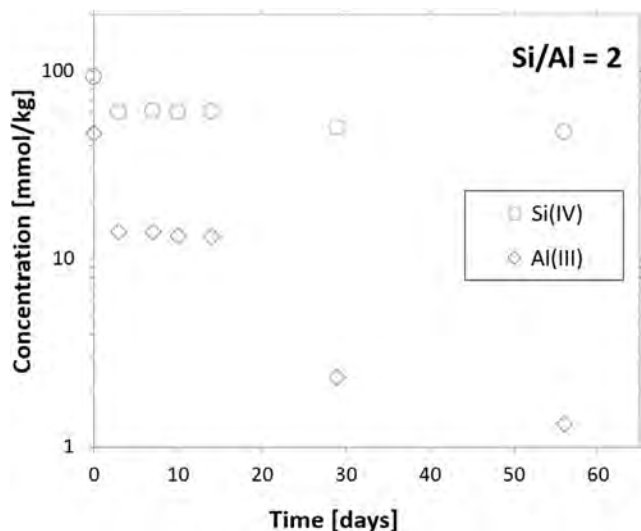


FIGURE 4 Changes in supernatant Si and Al concentrations over time for N–A–S–(H) reacted at 50°C with bulk Si/Al = 2.0. The error from triplicate measurements is smaller than the size of the symbol, so error bars are not shown [Color figure can be viewed at wileyonlinelibrary.com]

measurements. At Si/Al = 1.5, the plateau is visible between the 7 and 14-days measurements.

The solids precipitated from the Si/Al = 1 and Si/Al = 2 systems with supernatant concentrations shown in Figures 2 and 4 were triple-washed and freeze-dried and then analyzed by XRD to determine whether the rapid drops in Si and Al concentrations were accompanied by a structural change in the solids. Diffractograms for solids aged 3, 7, 10, 14, 28, and 56 days (the same time points for which concentrations are shown in Figures 2 and 4) with Si/Al = 1.0 and 2.0 are shown in Figures 5 and 6. Both samples are X-ray amorphous at early ages and developed clearly defined peaks as the reaction time increased. All peaks observed in both samples are attributed to Na-faujasite (pdf #00-012-0246; $\text{Na}_2\text{Al}_2\text{Si}_{2.4}\text{O}_{8.6}\cdot 6.7(\text{H}_2\text{O})$). This amorphous to crystalline transition is similar to that observed when zeolite synthesis is achieved by aging gels.²⁹

In the Si/Al = 1.0 system, the formation of crystalline faujasite began between 3 and 7 days, and fully defined peaks formed between 7 and 10 days (and remained through 56 days). This timing correlates closely with the rapid drop in Si(IV) and Al(III) concentrations shown for the Si/Al = 1.0 samples in Figure 2, which occurred between 7 and 10 days. Similarly, the development of faujasite XRD peaks visible in Figure 6 for the Si/Al = 2.0 sample corresponds closely in time with the decreased concentrations of Si(IV) and Al(III) shown in Figure 4 for the same system. In the Si/Al = 2.0 system, this transition occurred between 14 and 28 days. The rapid drop in concentrations observed in Si and Al concentrations is thus attributed to the formation of faujasite, which has a lower solubility than the

pseudo-equilibrium X-ray amorphous phase that caused the plateau in concentrations.

The discovery of the amorphous phase that appears to be at pseudo-equilibrium with the surrounding supernatant solution has significant implications with regard to developing kinetic models for the formation of N–A–S–(H). Specifically, this discovery emphasizes the importance of taking a stepwise approach to modeling these systems. Since the N–A–S–(H)

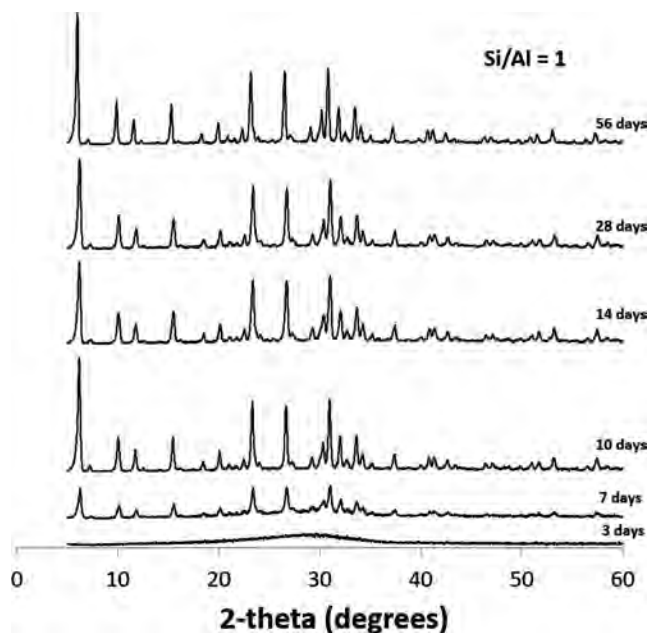


FIGURE 5 Temporal evolution of powder X-ray diffraction data for N–A–S–(H) reacted at 50°C with bulk Si/Al = 1. All peaks are attributed to faujasite (pdf #00-012-0246)

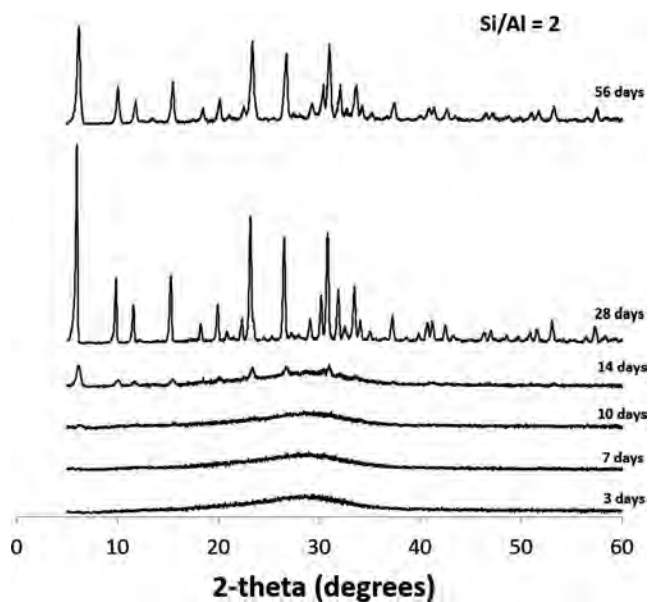


FIGURE 6 Temporal evolution of powder X-ray diffraction data for N–A–S–(H) reacted at 50°C with bulk Si/Al = 2. All peaks are attributed to faujasite (pdf #00-012-0246)

composition and structure, as well as the supernatant concentrations, change over time, a stepwise approach to modeling phase equilibria can account for the simultaneous increase in dissolved silicon and aluminum availability due to precursor dissolution and decrease in silicon and aluminum availability due to incorporation into the N–A–S–(H) solids. Since the amorphous N–A–S–(H) develops as a precursor to the crystalline N–A–S–(H), the pathway to amorphous N–A–S–(H) could be modeled first, and then the conditions reassessed to determine whether the conditions favor a transition to crystalline N–A–S–(H).

Evolution of the local molecular environments over time was monitored using ^{29}Si and ^{27}Al solid-state NMR to provide further insight into the initial N–A–S–(H) network formation and evolution as the samples reached equilibrium concentrations. In contrast to the XRD results, which are sensitive to long-range ordering, solid-state NMR is sensitive to short-range bonding and electronic environments, which enables the characterization of local molecular environments in both crystalline and amorphous materials. Figures 7 and 8 show the ^{29}Si solid-state single pulse NMR data from the same Si/Al = 1 and Si/Al = 2 specimens that were characterized by XRD at the respective time points.

After 3 days, the ^{29}Si spectra for both Si/Al = 1 and Si/Al = 2 show a broad distribution of ^{29}Si signal intensity centered around -80 and -85 ppm. These two signals are assigned to partially cross-linked $Q^2(1\text{Al})$ species and an overlapping distribution of partially cross-linked $Q^2(0\text{Al})$ and $Q^3(2\text{Al})$, respectively.³⁰ Here, $Q^n(m\text{Al})$ refers to a tetrahedral silicon atom that is covalently bonded through a bridging oxygen atom to n silicon or aluminum atoms, of

which m are aluminum. At longer times, that is, at 7 and 14 days in the Si/Al = 1 and 2 materials, respectively, signals are observed at -80 , -85 , and -89 ppm. The new signal at -89 ppm is assigned to an overlapping distribution of $Q^3(1\text{Al})$ and $Q^4(3\text{Al})$ species, while the narrow signal at -85 ppm is believed to be fully cross-linked $Q^4(4\text{Al})$, though further NMR experiments are required to verify the ^{27}Al – ^{29}Si connectivity.³¹ Longer times also resulted in narrower peak widths for the signals at -85 and -89 ppm, which is consistent with a narrower distribution of ^{29}Si sites in the N–A–S–(H) solids, such as would be present in a crystalline material. The narrowing of the ^{29}Si signals is accompanied by the observation of reflections in the XRD measurements, further corroborating the development of a more highly ordered network. At 28 days for each sample, there was a further decrease of the NMR peak widths, again indicating a narrower distribution of the ^{29}Si sites, consistent with a long-range ordered, crystalline material. In the case of the Si/Al = 2 solid, new signals arose at -94 , -99 , and -102 ppm. These three signals are assigned to $Q^4(2\text{Al})$, $Q^4(1\text{Al})$, and $Q^3(0\text{Al})$ species, respectively. The observation of these signals is consistent with the formation of a more highly coordinated ^{29}Si network in the N–A–S–(H) solids, again corroborated by the XRD reflections indicating a faujasite-like crystal structure.

Figure 9 shows the ^{27}Al solid-state single pulse NMR characterization for the Si/Al = 2 sample at the same time points as presented in Figure 8. The ^{27}Al spectra shown were similar under these field conditions, so only one set of spectra is shown as a representative of the ^{27}Al environment in the N–A–S–(H) solids.

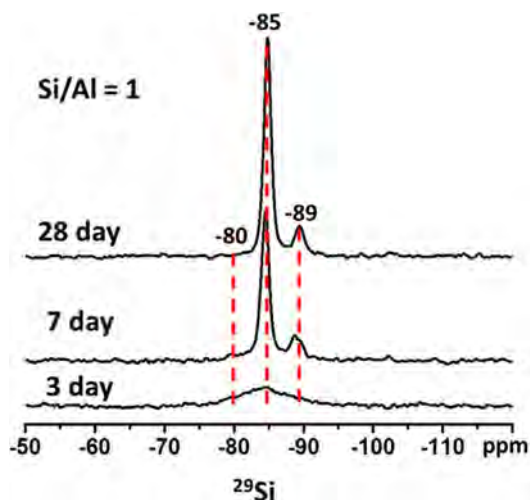


FIGURE 7 1D ^{29}Si solid-state single-pulse MAS nuclear magnetic resonance (NMR) of synthetic sodium aluminosilicate samples prepared from sodium silicate and aluminate solutions at 50°C with a starting molar ratio of Si/Al = 1 for samples allowed to react for three different time points as indicated on the spectra [Color figure can be viewed at wileyonlinelibrary.com]

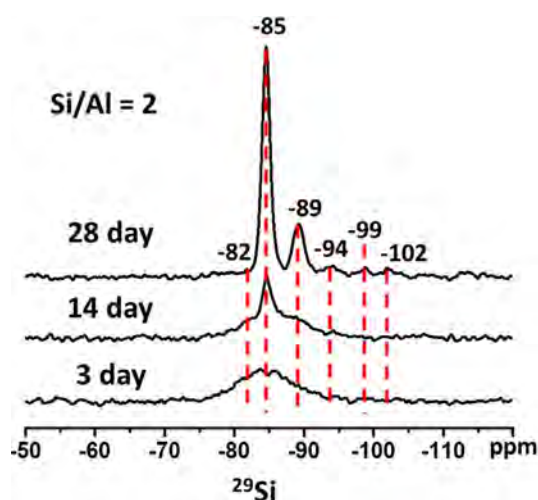


FIGURE 8 1D ^{29}Si solid-state single-pulse MAS nuclear magnetic resonance (NMR) of synthetic aluminosilicate samples prepared from sodium silicate and aluminate solutions at 50°C with a starting molar ratio of Si/Al = 2 for samples allowed to react for three different time points as indicated on the spectra [Color figure can be viewed at wileyonlinelibrary.com]

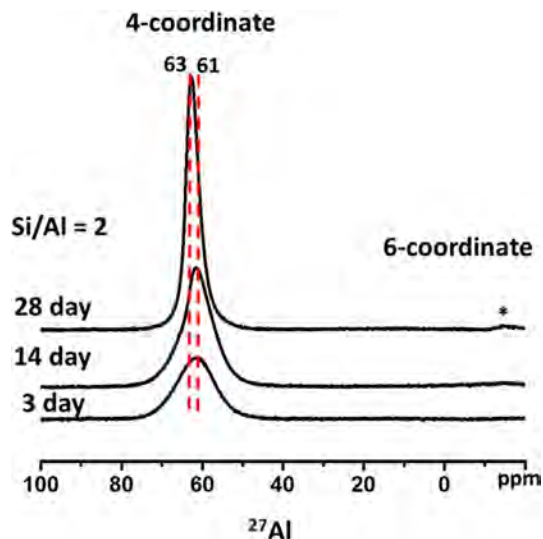


FIGURE 9 1D ^{27}Al solid-state single-pulse MAS nuclear magnetic resonance (NMR) of synthetic aluminosilicate samples prepared from sodium silicate and aluminate solutions at 50°C with a bulk molar ratio of $\text{Si}/\text{Al} = 2$ for samples allowed to react for 3, 14, and 28 d as indicated on the spectra. *indicates the spinning sideband signal present for the signals at ~ 60 ppm [Color figure can be viewed at wileyonlinelibrary.com]

In the 3-day sample, the ^{27}Al shows a broad distribution of signal intensity centered around 61 ppm. The signal at 61 ppm can be attributed to 4-coordinate ^{27}Al sites, which are ^{27}Al species that are incorporated into tetrahedral bonding networks.³² As time elapsed, a narrowing of the signal peak width is observed, indicating a narrower distribution of ^{27}Al sites, consistent with the long-range order observed by XRD, and a small shift in the position by approximately 2 ppm to higher frequency is observed. Measurements at higher magnetic fields are required to discern more subtle changes in the ^{27}Al 4-coordinate species observed in the solids.

The ^{29}Si and ^{27}Al solid-state NMR data from the N–A–S–(H) solids at different times provide detailed information regarding the evolution of local molecular structure. The ^{29}Si and ^{27}Al NMR spectra show signals that are consistent with the formation of an initially amorphous, partially cross-linked aluminosilica network that condenses as time increases into a more highly coordinated network structure consistent with that of faujasite. Although the XRD measurements show a crystalline faujasite phase with no noticeable changes at later times, the ^{29}Si 1D NMR shows significant changes in the local molecular structure as aging continues, indicating that the network is still changing over time.

3.2 | Equilibrium N–A–S–(H) aqueous chemistry and solid composition

Given the insubstantial changes in solution composition and N–A–S–(H) structure between 28 and 56 days, it is assumed

that the N–A–S–(H) has reached equilibrium with the supernatant solution at 56 days, so the equilibrium solution and solid-state compositions were evaluated further for 56-day samples. Equilibrium supernatant concentrations for samples reacted at 50°C for 56 days with bulk Si/Al (molar) ranging from 1.0 to 2.0 are shown in Figure 10. Error bars show the range of measured concentrations from independent batch reactors prepared with independent stock solutions. For $\text{Si}/\text{Al} = 1$ and 2, three replicate reactors were analyzed, and for $\text{Si}/\text{Al} = 1.5$, two replicate reactors were analyzed. As bulk molar Si/Al increased from 1 to 2, supernatant Si concentrations increased somewhat linearly from 10.4 to 48.0 mmol/kg, and Al concentrations decreased from 7.56 to 1.63 mmol/kg. It should be noted that bulk Si/Al ratios were manipulated by adjusting the bulk Al(III) in each sample, so at lower Si/Al ratios, bulk Al(III) concentrations were highest.

Thermogravimetric data for N–A–S–(H) solids synthesized with bulk $\text{Si}/\text{Al} = 1, 1.5,$ and 2 reacted at 50°C for 56 days are shown in Figure 11. All of the samples showed continuous mass loss with peaks centered at 150°C to 200°C . The mass losses correspond to a loss in evaporable and non-evaporable water, and total mass loss increased with increasing age for all samples. There was no systematic variation in the temperature at which peak mass loss occurred (ie, the temperature at which the derivative of mass loss curve was the most negative) across bulk compositions and no substantial difference in total water loss across bulk compositions. All of the mass losses for all samples occurred between 40°C and approximately 400°C . Peak mass loss is generally observed between 175°C and 400°C for faujasite,³³ so the TGA data are consistent with the XRD data in Figures 5 and 6. Furthermore, Musyoka et al³⁴ found peak mass loss for zeolite-X, a type of faujasite, to be between 150°C and 200°C . As discussed later in this section, the faujasite precipitated in the study presented here is believed to be zeolite-X, so the

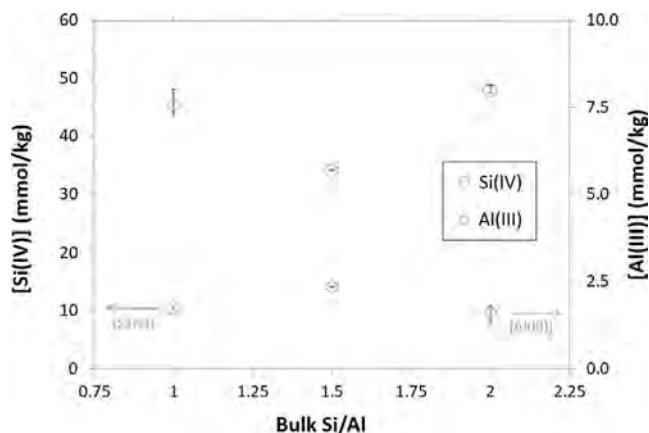


FIGURE 10 N–A–S–(H) equilibrium Si and Al concentrations versus bulk Si/Al molar ratios for N–A–S–(H) reacted at 50°C for 56 d [Color figure can be viewed at wileyonlinelibrary.com]

FIGURE 11 Thermogravimetric analysis data for N-A-S-(H) samples reacted at 50°C for 56 d with bulk Si/Al = 1, 1.5, and 2

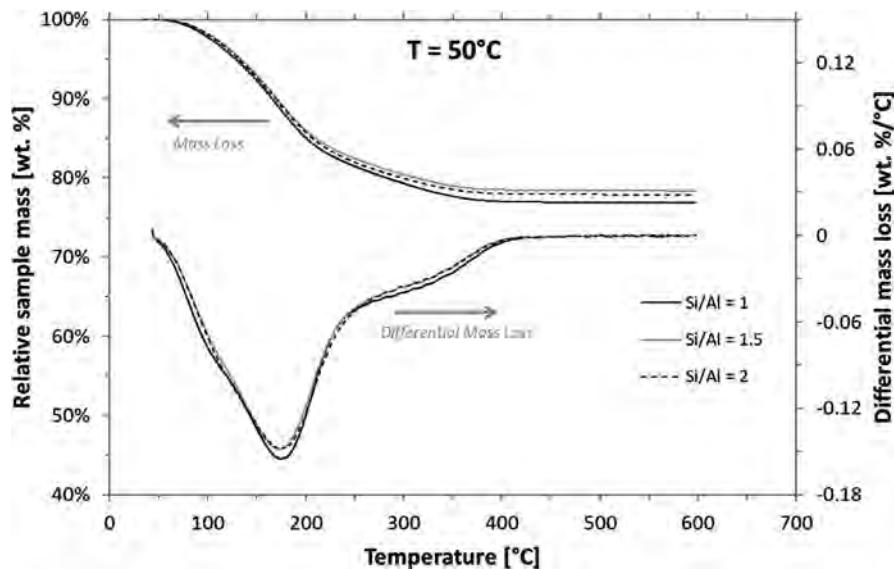


TABLE 1 Composition of N-A-S-(H) phases reacted for 56 d at 50°C with bulk Si/Al = 1 to 2

Bulk Si/Al ratio (molar)	N-A-S-(H) composition
1	$\text{NaAlSi}_{0.98}\text{O}_{3.96} \cdot (\text{H}_2\text{O})_{2.35}$
1.5	$\text{NaAlSi}_{0.99}\text{O}_{3.98} \cdot (\text{H}_2\text{O})_{2.16}$
2	$\text{NaAlSi}_{1.01}\text{O}_{4.03} \cdot (\text{H}_2\text{O})_{2.23}$

peak mass loss between 150°C and 200°C found in this study is consistent with the literature.

Table 1 shows the compositions of the solid N-A-S-(H) phases reacted for 56 days at 50°C with bulk Si/Al molar ratios of 1, 1.5, and 2. The Al_2O_3 and SiO_2 stoichiometric coefficients shown in Table 1 were calculated by subtracting the equilibrium concentrations of Al and Si from the bulk concentrations. Each value represents the average concentration calculated from the same two or three independent samples whose supernatant concentrations are reported in Figure 10.

The Na_2O stoichiometric coefficients could not be calculated in the same way because the changes in aqueous sodium concentrations were smaller than the measurement error due to the high sodium concentrations. Instead, the molar fractions were determined by charge balance to be equal to the molar fraction of Al_2O_3 for each sample (ie, $\text{Na}_2\text{O}/\text{Al}_2\text{O}_3 = 1$) since sodium is present as a charge balancing cation to alumina tetrahedra, which carry a -1 charge.² The molar water content was calculated from the measured TGA mass loss (Figure 11) for a single sample at each concentration, and the stoichiometric coefficients for water shown in Table 1 represent these measured values. Estimated absolute errors in Si/Al ratios are 0.01 based on the range of Si and Al supernatant concentrations measured (Figure 10). Estimated absolute errors in the $\text{H}_2\text{O}/\text{Al}$ ratios are ± 0.2 units, consistent with the study by Myers et al.³⁵

To validate the solid composition measurements, a separate series of N-A-S-(H) samples was prepared in the same way as those described previously and analyzed by acid digestion followed by ICP analysis of the resulting solution. The Si/Al ratios determined by mass balance (the same way as the values presented in Table 1) varied from the Si/Al ratios determined by acid digestion by less than 1% for all three samples analyzed in this way. The assumed sodium concentrations could not be validated in the same way due to complications resulting from the complex matrix in the digested samples, which was composed of hydrofluoric acid as well as a buffer solution composed of triethanolamine and triethylenetetramine used to neutralize the acid prior to ICP analysis.

As shown in Table 1, there was only a slight increase in N-A-S-(H) Si/Al ratio as the bulk Si/Al ratio increased from 1 to 2, and the difference between all N-A-S-(H) Si/Al ratios was less than the estimated error. The Si/Al molar ratio in all solid N-A-S-(H) phases was close to 1, regardless of the bulk Si/Al ratio. Others have described three different framework units that make up inorganic polymers: poly(sialate) ($-\text{Si}-\text{O}-\text{Al}-\text{O}-$), corresponding to N-A-S-(H) Si/Al = 1; poly(silate-siloxo) ($\text{Si}-\text{O}-\text{Al}-\text{O}-\text{Si}-\text{O}-$), corresponding to N-A-S-(H) Si/Al = 2; and poly(sialate-disiloxo) ($\text{Si}-\text{O}-\text{Al}-\text{O}-\text{Si}-\text{O}-\text{Si}-\text{O}-$) groups, corresponding to N-A-S-(H) Si/Al = 3.^{36,37} Although Al-O-Al bonds are not favored according to Loewenstein's principal,³⁸ such bonds are possible if sufficient aluminum is present in the pore solution.²⁴ Here, since the N-A-S-(H) Si/Al ratio is close to one for all samples, it is presumed that poly(sialate) units dominate.

Based on the N-A-S-(H) composition presented here and the XRD diffractograms in Figures 5 and 6, a further discussion of characterization of the N-A-S-(H) is warranted. Figures 5 and 6 show that the N-A-S-(H) reacted for 56 days with bulk Si/Al = 1 and 2 has a crystalline

structure resembling that of faujasite. Faujasite is a zeolitic phase composed of sodalite cages connected by hexagonal prisms and can be split generally into two types based on its Si/Al ratio.³⁹ Faujasite with a molar Si/Al ratio less than 1.5 is referred to as zeolite-X, while faujasite with a molar Si/Al greater than 1.5 is referred to as zeolite-Y.⁴⁰ Since the Si/Al ratio in the present study was close to 1 for all bulk Si/Al compositions (Table 1), the faujasite is classified as zeolite-X. The 1D ²⁹Si NMR spectra also corroborate the formation of zeolite-X based on the previously assigned signals.

Other researchers have successfully synthesized zeolite-X in the laboratory by combining solutions of sodium silicate and sodium aluminate. Buchwald et al⁴¹ found that zeolite-A, zeolite-X, and sodalite can form separately or coexist in different combinations depending on the synthesis conditions, and the concentration of NaOH is the most important factor in determining which phases form. At 1 M NaOH, the Buchwald et al⁴¹ study found that zeolite-X with Si/Al = 1 was the preferred phase regardless of bulk Si/Al ratio, consistent with the findings of the study presented here. Hajimohammadi et al⁴² previously observed the formation of Na-faujasite in synthetic inorganic polymers formed by mixing amorphous silica with sodium aluminate at 40°C, and Fletcher et al³⁶ detected an unnamed crystalline zeolite in a metakaolin-based inorganic polymer with bulk Si/Al = 1.

It should be noted that fly ash Si/Al ratio is an important parameter with regard to IPB performance beyond its effect on N-A-S-(H) Si/Al ratio. Most notably, it has been shown to affect dissolution rates of fly ash,⁵ in turn impacting the transient concentrations of available silicon and aluminum to form the binding N-A-S-(H) phase. Bulk Si/Al ratios have also been shown to impact the microstructure of mature IPB in the case of metakaolin-based systems,⁸ so composition of the N-A-S-(H) is not the only factor impacting mechanical properties.

3.3 | Effect of silicate activator Si/Na ratio on N-A-S-(H) composition

To test the impact of silicate solution Si/Na on N-A-S-(H) Si/Al ratio, a series of N-A-S-(H) solids were synthesized following the same procedure used for the experiments described previously, but with the silicate stock solution Si/Na molar ratio varying from 0.1 to 1.0 and bulk Si/Al varying from 0.89 to 9.58. The silicate stock solution Si/Na in the experiments described previously was held constant at 0.1. Here, the range of Si/Na values in the silicate-activating solution was chosen to match the common range of silicate activators used in alkali-activated fly ash systems. The same sodium aluminate stock solution (0.1 M sodium aluminate) was used in this experiment as in the previous experiments. In these experiments, the samples were reacted at 50°C for 56 days.

Table 2 shows the Si/Al molar ratio of the solids increasing from 1.10 to 2.39 as the Si/Na molar ratio of the silicate stock

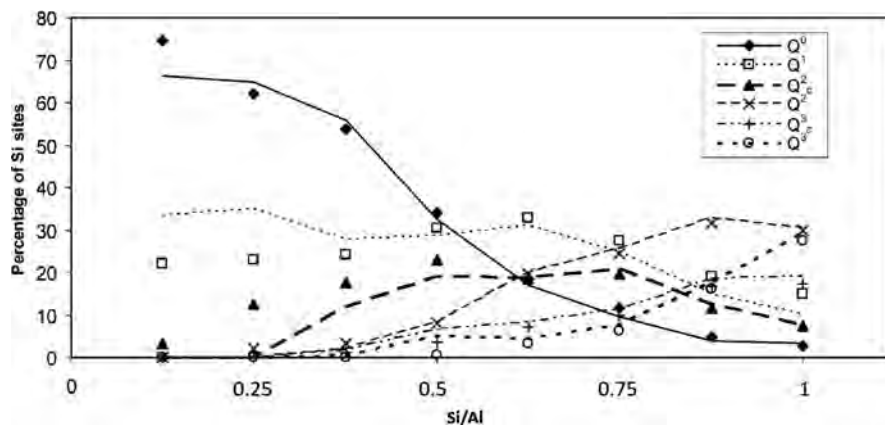
TABLE 2 Si/Al molar ratios in N-A-S-(H) reacted at 50°C for 56 d with sodium silicate Si/Na molar ratios varying from 0.10 to 1.05 and bulk Si/Al ratios varying from 0.89 to 9.58

Si Solution Si/Na	Bulk Si/Al	N-A-S-(H) Si/Al
0.10	0.89	1.10
0.20	1.86	1.30
0.51	4.83	1.90
0.77	7.04	2.17
1.05	9.58	2.39

solution increased from 0.10 to 1.05. While the highest bulk Si/Al ratio in this experiment (9.58) was much higher than in the first set of experiments, it is worth noting that, even with an increase in the bulk Si/Al molar ratio from 0.89 to 1.86, the N-A-S-(H) solid's Si/Al molar ratio increased from 1.10 to 1.30 when it was accompanied by an increase in the Si Solution Si/Na ratio. This is noteworthy because in the previous experiments conducted with the Si/Na ratio held constant at 0.10, increasing bulk Si/Al from 1 to 2 did not change the N-A-S-(H) Si/Al (constant at approximately 1.0, Table 1). Here, with a similar increase in bulk Si/Al ratio but with Si/Na also increasing from 0.10 to 0.20 rather than remaining constant, there was a significant increase in the solid N-A-S-(H) Si/Al ratio, indicating an increase in the frequency of Si-O-Si type bonds compared to the frequency of Si-O-Al type bonds.

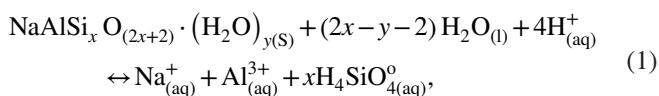
In alkali-activated systems, it is well-known that the concentration of silicates in the sodium hydroxide/sodium silicate-activating solution can greatly impact the microstructure and thus the engineering properties of the binder. The initial speciation of the silicates in sodium silicate-activating solution is highly complex and greatly impacts the network formation and structure (see Figure 12). The properties of sodium silicate solutions, including viscosity and speciation of silicates, are highly dependent on the Si/Na ratio of the solution.^{25,43} As Si/Na increases, the number of Q⁰ and Q¹ Si sites (monomeric and dimeric silicates) in the solution decreases rapidly.²⁵ This can cause a large change in N-A-S-(H) microstructure,² as aluminate anions react preferentially with silicate anions of lower connectivity.⁴⁴ Additionally, the formation of dissolved oligomers of silicates in the silicate-activating solution leaves fewer bonding sites on the silicate chains. Duxson et al² state that silicate speciation in the activating solution is probably more important than the absolute silicate concentration in determining N-A-S-(H) microstructure. The findings here support that claim, as changes in bulk Si/Al ratio had little effect on the N-A-S-(H) composition, while increasing silicate solution Si/Na ratio had a significant impact on the N-A-S-(H) composition. Since these tests were only done to determine if changes in solution composition impacted the solid composition, solubility products were not determined. More work is needed to better characterize the impact of changes in Si/Na ratio in the future.

FIGURE 12 Silica speciation in sodium silicate solutions with varying Si/Na ratios. Reprinted (adapted) with permission from [25]. Copyright 2005 American Chemical Society



3.4 | Calculation of solubility products for N–A–S–(H) phases

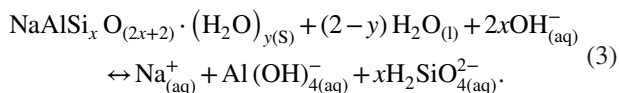
Solubility products (K_{sp}) were calculated for each of the N–A–S–(H) solids with the bulk compositions shown in Table 1. The dissolution reaction assumed to calculate solubility products is shown in Equation 1:



where x is the Si/Al molar ratio of the solids and y is the stoichiometric coefficient of H_2O in the solids. This convention of calculating solubility products follows the convention presented by Sposito⁴⁵ for clays. Following the reaction in Equation 1, equilibrium solubility products were calculated with Equation 2:

$$K_{sp} = \left\{ \text{Na}^+_{(\text{aq})} \right\} \cdot \left\{ \text{Al}^{3+}_{(\text{aq})} \right\} \cdot \left\{ \text{H}_4\text{SiO}^0_{4(\text{aq})} \right\}^x \cdot \left\{ \text{H}^+_{(\text{aq})} \right\}^{-4} \cdot \left\{ \text{H}_2\text{O}_{(\text{l})} \right\}^{-(y-2x+2)} \quad (2)$$

Equilibrium constants were also calculated based on the dissolution reaction shown in Equation 3:



Equation 3, in contrast to Equation 1, shows OH^- as a reactant to represent the alkaline conditions present in the study, and uses the dominant aluminum and silicon species expected at high pH. Following the reaction presented in Equation 3, equilibrium products were calculated using Equation 4:

$$K_{sp} = \left\{ \text{Na}^+_{(\text{aq})} \right\} \cdot \left\{ \text{Al}(\text{OH})^-_{4(\text{aq})} \right\} \cdot \left\{ \text{H}_2\text{SiO}^{2-}_{4(\text{aq})} \right\}^x \cdot \left\{ \text{OH}^-_{(\text{aq})} \right\}^{-2x} \cdot \left\{ \text{H}_2\text{O}_{(\text{l})} \right\}^{(y-2)} \quad (4)$$

Activities of $\text{Na}^+_{(\text{aq})}$, $\text{Al}^{3+}_{(\text{aq})}$, $\text{H}_4\text{SiO}^0_{4(\text{aq})}$, $\text{H}^+_{(\text{aq})}$, and $\text{H}_2\text{O}_{(\text{l})}$ were determined with PHREEQC using the measured supernatant concentrations of $\text{Na}_{(\text{aq})}$, $\text{Si(IV)}_{(\text{aq})}$, and $\text{Al(III)}_{(\text{aq})}$ with the pH calculated from charge balance. The Truesdell-Jones version of the extended Debye-Hückel equation was used within PHREEQC with the LLNL database to determine the activity coefficients of each species, shown in Equation 5:

$$\log \gamma_i = \frac{-Az_i^2 \sqrt{I}}{1 + B\alpha_i \sqrt{I}} + bI, \quad (5)$$

where γ_i is the activity coefficient of ion “ i ,” A and B are Debye-Hückel parameters based on the dielectric constant of water and the temperature, z_i is the ion valence, α_i is a parameter accounting from the ionic radius, b is an empirical parameter, and I is the ionic strength of the solution. The activities of species for each sample, as well as the ionic strength and pH, can be found in the Supporting Information.

The calculated solubility constants for N–A–S–(H) solids reacted at 50°C with bulk Si/Al ratios varying from 1.0 to 2.0 and average solid compositions from Table 1 are shown in Table 3. An absolute error of 0.2 log units was determined by varying all of the inputs in Equations 2 and 4 within their respective error ranges to determine the maximum and minimum value of K_{sp} and K_{eq} that could be achieved with all of the inputs staying within their respective error bounds. Calculated K_{sp} and K_{eq} values do not vary significantly with bulk Si/Al ratio.

Comparison of our results with previous work shows consistency among different researchers; however, it also highlights the importance of ensuring adequate equilibration times. For example, Gómez-Zamorano et al¹⁸ evaluated the solubility using alternative product species (AlO^{2-} vs AlO^{3+}). Transforming their $\log K_{sp}$ to the form used in Equation 3 yields a value of 11.8. This slightly higher value reported by Gómez-Zamorano et al¹⁸ is likely due to the extended reaction time utilized in our experiments. Indeed, our data suggest that about 56 days were required to reach

Bulk Si/Al	N-A-S-(H) composition	Log K_{sp}	Log K_{eq}
1	NaAlSi _{0.98} O _{3.96} •(H ₂ O) _{2.35}	11.2 ± 0.2	-5.70 ± 0.2
1.5	NaAlSi _{0.99} O _{3.98} •(H ₂ O) _{2.16}	11.1 ± 0.2	-5.74 ± 0.2
2	NaAlSi _{1.01} O _{4.03} •(H ₂ O) _{2.23}	11.0 ± 0.2	-5.78 ± 0.2

TABLE 3 Solubility products (K_{sp}) and equilibrium constants (K_{eq}) of N-A-S-(H) reacted at 50°C with Si/Al = 1, 1.5, and 2 calculated using Equations 2 and 4, respectively

apparent equilibrium. Nonetheless, the values are reasonably consistent.

Lothenbach et al⁴⁶ measured the solubility of zeolite-X with a slightly different composition than that examined here, Si/Al = 1.25, and at 25°C. Applying our composition values to their stoichiometry, we are within 26% of their value. While these values are remarkably similar, it is important to note that the experiments were conducted at different temperatures.

Zeolite-X solubility was also calculated previously by Šefčík et al⁴⁷ from experimental data obtained from a separate study by Čizmek et al.⁴⁸ In the latter experiments, zeolite-X precipitated from a mixture of sodium hydroxide, sodium silicate, and aluminum trihydrate with Si/Al = 2 was rinsed and dissolved in 2 M sodium hydroxide at 80°C (compared to the 50°C reaction temperature in the present study). The values from Šefčík et al⁴⁵ and Čizmek et al⁴⁸ cannot be directly compared to the values determined here because of the large temperature differences, and Šefčík et al⁴⁷ used concentrations rather than activities in their calculations, neglecting ionic strength effects. Ionic strength effects are far from negligible since the solution concentrations are so high in both studies.

In addition to the solubility products and equilibrium constants presented for the equilibrated crystalline phases presented in Table 3, equilibrium constants were determined for the amorphous N-A-S-(H) phases using the 7-day Si(IV) and Al(III) concentrations presented in Figures 2–4. Equilibrium constants were calculated using Equation 4, corresponding to the reaction presented in Equation 2, which uses the dominant species of Si(IV) and Al(III) rather than the Sposito⁴⁵ convention. Using Si(IV) and Al(III) to determine equilibrium constants allows for a stronger correlation with total Si(IV) and Al(III) concentrations to better understand the relationship between the amorphous and crystalline N-A-S-(H) solids. It should be noted that supernatant Na⁺ concentrations and water content were not measured for the amorphous phases, as the original intent of this study was to understand the equilibrium conditions. As such, to calculate amorphous phase solubility products, 1000 mmol/kg was assumed for the Na⁺ supernatant concentrations, and the water contents were set equal to the same water contents measured in the analogous crystalline phases. While these assumptions may not be 100% accurate, deviations in these values have relatively little impact on the amorphous phase equilibrium constants. The equilibrium products for N-A-S-(H) reacted with Si/Al = 1, 1.5, and 2 for 7 and 56 days are presented in Table 4.

The amorphous N-A-S-(H) equilibrium products are approximately two orders of magnitude higher than the crystalline N-A-S-(H) equilibrium products, indicating that the amorphous N-A-S-(H) is more soluble than the crystalline N-A-S-(H) under the conditions studied here. There is no significant change in amorphous N-A-S-(H) solubility with bulk Si/Al, suggesting that a single amorphous phase precipitates at 50°C when bulk Si/Al varies between 1 and 2.

4 | CONCLUSIONS

This study analyzed the relationship between the aqueous chemistry and the resultant composition and structure of solids for N-A-S-(H) phases synthesized at a constant temperature. It was shown that early N-A-S-(H) products are X-ray amorphous, but a transition to an XRD-verified crystalline structure, specifically faujasite, occurs after several weeks to several months, depending on the equilibration temperature. Both ²⁹Si and ²⁷Al NMR spectra collected as a function of time (up to 28 days) supported the XRD results indicating that the initial amorphous, partially cross-linked aluminosilica network condensed to a more highly coordinated network structure.

The bulk Si/Al ratio was shown to have little impact on N-A-S-(H) solid Si/Al ratio when synthesized using sodium silicate solutions with Si/Na ratios low enough that all silicate species are monomeric. Only slight changes in sodium silicate Si/Na ratio were shown to have a significant impact on the N-A-S-(H) Si/Al ratio, an important finding that has implications for the understanding and optimization of activator solution chemistries. Additionally, solubility products of N-A-S-(H) were calculated for a range of compositions, and these values will allow for thermodynamic modeling of N-A-S-(H) systems, which can have a substantial impact on our ability to predict engineering properties for these

TABLE 4 Equilibrium products of crystalline N-A-S-(H) reacted for 56 d and amorphous N-A-S-(H) reacted for 7 d

Bulk Si/Al	Log K_{eq}	
	Crystalline N-A-S-(H)	Amorphous N-A-S-(H)
1	-5.71	-3.10
1.5	-5.74	-3.15
2	-5.78	-3.13

cementitious binders. Finally, amorphous phase equilibrium constants were determined, and, as expected, the amorphous N–A–S–(H) is more soluble than its crystalline counterpart as evident by the approximately 2.6 order of magnitude difference in $\log K_{sp}$ values. The results provide important insights into the early formation of aluminosilicates, which are relevant to determining appropriate design parameters for IPBs.

ACKNOWLEDGMENTS

The authors thank Philip Bennett and Aditya Kumar for their assistance in developing the experimental methods presented in this study. The authors also thank Michelle Lacks, Kevin Folliard, Victoria Ibarra, Phil Tomlin, Michael Williams, and Lamont Prosser for their support. Federal Highway Administration's Exploratory Advanced Research Program provided financial support for the study presented in this paper through Project DTFH61-13-H-00011, for which the authors are also grateful.

ORCID

Maria C. G. Juenger  <https://orcid.org/0000-0001-9282-3298>

REFERENCES

- Fernández-Jiménez A, Palomo A, Criado M. Microstructure development of alkali-activated fly ash cement: a descriptive model. *Cem Concr Res*. 2005;35(6):1204–9.
- Duxson P, Fernández-Jiménez A, Provis JL, Lukey GC, Palomo A, Deventer JSJ. Geopolymer technology: the current state of the art. *J Mater Sci*. 2006;42(9):2917–33.
- Davidovits J. High-alkali cements for 21st century concretes. In: Mehta PK, editor. *Concrete technology: past, present, and future*. Farmington Hills, Michigan: American Concrete Institute, 1994; p.383–98.
- Aughenbaugh KL, Williamson T, Juenger MCG. Critical evaluation of strength prediction methods for alkali-activated fly ash. *Mater Struct Constr*. 2015;48(3):607–20.
- Duxson P, Provis JL. Designing precursors for geopolymer cements. *J Am Ceram Soc*. 2008;91(12):3864–9.
- de Vargas AS, Dal Molin DCC, Vilela ACF, Da SFJ, Pavão B, Veit H. The effects of $\text{Na}_2\text{O}/\text{SiO}_2$ molar ratio, curing temperature and age on compressive strength, morphology and microstructure of alkali-activated fly ash-based geopolymers. *Cem Concr Compos*. 2011;33(6):653–60.
- Xu H, Van Deventer JSJ. The geopolymerisation of aluminosilicate minerals. *Int J Miner Process*. 2000;59(3):247–66.
- Duxson P, Provis JL, Lukey GC, Mallicoat SW, Kriven WM, van Deventer JSJ. Understanding the relationship between geopolymer composition, microstructure and mechanical properties. *Colloids Surfaces A Physicochem Eng Asp*. 2005;269(1–3):47–58.
- Barbosa VFF, MacKenzie KJD, Thaumaturgo C. Synthesis and characterisation of materials based on inorganic polymers of alumina and silica: sodium polysialate polymers. *Int J Inorg Mater*. 2000;2(4):309–17.
- Fernández-Jiménez A, Palomo A, López-Hombrados C. Engineering properties of alkali-activated fly ash concrete. *ACI Mater J*. 2006;103(2):106–12.
- Zhang Y, Sun W, Li Z. Infrared spectroscopy study of structural nature of geopolymeric products. *J Wuhan Univ Technol Sci Ed*. 2008;23(4):522–7.
- Bernal SA, Provis JL. Durability of alkali-activated materials: progress and perspectives. *J Am Ceram Soc*. 2014;97(4):997–1008.
- Fernández-Jiménez A, García-Lodeiro I, Palomo A. Durability of alkali-activated fly ash cementitious materials. *J Mater Sci*. 2006;42(9):3055–65.
- García-Lodeiro I, Palomo A, Fernández-Jiménez A. Alkali-aggregate reaction in activated fly ash systems. *Cem Concr Res*. 2007;37(2):175–83.
- Miranda JM, Fernández-Jiménez A, González JA, Palomo A. Corrosion resistance in activated fly ash mortars. *Cem Concr Res*. 2005;35(6):1210–7.
- Williamson T, Juenger MCG. The role of activating solution concentration on alkali-silica reaction in alkali-activated fly ash concrete. *Cem Concr Res*. 2016;83:124–30.
- Provis JL, Palomo A, Shi C. Advances in understanding alkali-activated materials. *Cem Concr Res*. 2015;78:110–25.
- Gomez-Zamorano L, Balonis M, Erdemli B, Neithalath N, Sant G. C-(N)-S-H and N-A-S-H gels: Compositions and solubility data at 25°C and 50°C. *J Am Ceram Soc*. 2017;100(6):2700–11.
- Fernández-Jiménez A, Palomo A, Sobrados I, Sanz J. The role played by the reactive alumina content in the alkaline activation of fly ashes. *Microporous Mesoporous Mater*. 2006;91(1–3):111–9.
- Duxson P, Mallicoat SW, Lukey GC, Kriven WM, van Deventer JSJ. The effect of alkali and Si/Al ratio on the development of mechanical properties of metakaolin-based geopolymers. *Colloids Surfaces A Physicochem Eng Asp*. 2007;292(1):8–20.
- Oelkers EH, Schott J, Devidal J-L. The effect of aluminum, pH, and chemical affinity on the rates of aluminosilicate dissolution reactions. *Geochim Cosmochim Acta*. 1994;58(9):2011–24.
- Williamson T, Han J, Katz L, Sant G, Juenger MCG. Method for experimentally determining N-A-S-H solubility. *RILEM Tech Lett*. 2019;3:104–13.
- Rowles M, O'Connor B. Chemical optimisation of the compressive strength of aluminosilicate geopolymers synthesised by sodium silicate activation of metakaolinite. *J Mater Chem*. 2003;13(5):1161–5.
- Duxson P, Lukey GC, Separovic F, van Deventer JSJ. Effect of alkali cations on aluminum incorporation in geopolymeric gels. *Ind Eng Chem Res*. 2005;44(4):832–9.
- Provis JL, Duxson P, Lukey GC, Separovic F, Kriven WM, Van DJSJ. Modeling speciation in highly concentrated alkaline silicate solutions. *Ind Eng Chem Res*. 2005;44:8899–908.
- Hardjito D, Cheak CC, Lee Ing CH. Strength and setting times of low calcium fly ash-based geopolymer mortar. *Mod Appl Sci*. 2008;2(4):3–11.
- Muñiz-Villarreal MS, Manzano-Ramírez A, Sampieri-Bulbarela S, Gasca-Tirado JR, Reyes-Araiza JL, Rubio-Ávalos JC, et al. The effect of temperature on the geopolymerization process of a metakaolin-based geopolymer. *Mater Lett*. 2011;65(6):995–8.
- Abdullah MMA, Kamarudin H, Bhussain M, Khairul Nizar I, Rafiza AR, Zarina Y. The relationship of NaOH molarity, $\text{Na}_2\text{SiO}_3/\text{NaOH}$ ratio, fly ash/alkaline activator ratio, and curing temperature to the strength of fly ash-based geopolymer. *Adv Mater Res*. 2011;328–330:1475–82.

29. Katović A, Subotić B, Šmit I, Despotović LA, Ćurić M. Role of gel aging in zeolite crystallization. In: Ocelli R, editor. Zeolite synthesis. Washington D.C. American Chemical Society; 1989: p. 124–39.
30. Thompson JG. ^{29}Si and ^{27}Al nuclear magnetic resonance spectroscopy of 2:1 clay minerals. *Clay Miner.* 1984;19:229–36.
31. Engelhardt G, Lohse U, Samoson A, Mägi M, Tarmak M, Lippmaa E. High resolution ^{29}Si n.m.r. of dealuminated and ultrastable Y-zeolites. *Zeolites.* 1982;2(1):59–62.
32. Ray GJ, Meyers BL, Marshall CL. ^{29}Si and ^{27}Al n.m.r study of steamed faujasites—evidence for non-framework tetrahedrally bound aluminium. *Zeolites.* 1987;7(4):307–10.
33. Földvári M. Handbook of the thermogravimetric system of minerals and its use in geological practice. *Central Eur Geol.* 2011;213:106.
34. Musyoka NM, Petrik LF, Hums E, Kuhnt A, Schwieger W. Thermal stability studies of zeolites A and X synthesized from South African coal fly ash. *Res Chem Intermed.* 2015;41(2):575–82.
35. Myers RJ, L'Hôpital E, Provis JL, Lothenbach B. Effect of temperature and aluminium on calcium (alumino)silicate hydrate chemistry under equilibrium conditions. *Cem Concr Res.* 2015;68:83–93.
36. Fletcher RA, MacKenzie KJD, Nicholson CL, Shimada S. The composition range of aluminosilicate geopolymers. *J Eur Ceram Soc.* 2005;25(9):1471–7.
37. Davidovits J. Geopolymers: Inorganic polymeric new materials. *J Therm Anal.* 1991;37(8):1633–56.
38. Provis JL. Geopolymers and other alkali activated materials: why, how, and what? *Mater Struct.* 2013;47(1–2):11–25.
39. Ozdemir OD, Pişkin S. Zeolite X synthesis with different sources. *Int J Chem Environ Biol Sci.* 2013;1(2):229–32.
40. Lutz W. Zeolite Y: synthesis, modification, and properties—a case revisited. *Adv Mater Sci Eng.* 2014;2014:1–20.
41. Buchwald A, Zellmann HD, Kaps C. Condensation of aluminosilicate gels—model system for geopolymer binders. *J Non Cryst Solids.* 2011;357(5):1376–82.
42. Hajimohammadi A, Provis JL, van Deventer JSJ. Time-resolved and spatially-resolved infrared spectroscopic observation of seeded nucleation controlling geopolymer gel formation. *J Colloid Interface Sci.* 2011;357(2):384–92.
43. Iler RK. The chemistry of silica. New York, NY: John Wiley and Sons; 1979.
44. McCormick AV, Bell AT, Radke CJ. Multinuclear NMR investigation of the formation of aluminosilicate anions. *J Phys Chem.* 1989;93(5):1741–4.
45. Sposito G. The chemistry of soils. New York, NY: Oxford University Press; 1989: pp. 86–90.
46. Lothenbach B, Bernard E, Mader U. Zeolite formation in the presence of cement hydrates and albite. *Phys Chem Earth.* 2017;99:77–94.
47. Šefčík J, McCormick AV. Prediction of crystallization diagrams for synthesis of zeolites. *Chem Eng Sci.* 1999;54(15–16):3513–9.
48. Čizmek A, Komunjer L, Subotić B, Široki M, Rončević S. Kinetics of zeolite dissolution. Part 2. Dissolution of zeolite X in hot sodium hydroxide solutions. *Zeolites.* 1991;11(8):810–5.

SUPPORTING INFORMATION

Additional supporting information may be found online in the Supporting Information section.

How to cite this article: Williamson T, Katz LE, Han J, et al. Relationship between aqueous chemistry and composition, structure, and solubility of sodium aluminosilicate hydrates. *J Am Ceram Soc.* 2020;103:2160–2172. <https://doi.org/10.1111/jace.16868>

Table S1: Reactions and constants used for modeling taken from the LLNL database from PHREEQC

Reaction	Log k	ΔH (kJ/mol)
$H_2O = OH^- + H^+$	-14.00	55.81
$H_2O + Al^{3+} = AlO_2^- + 4H^+$	-22.88	180.90
$2H_2O + Na^+ + Al^{3+} = NaAlO_2 + 4H^+$	-23.63	190.33
$2H_2O + Al^{3+} = HAlO_2$	-16.43	144.70
$2H_2O + Al^{3+} = Al(OH)_2^+ + 2H^+$	-10.59	98.28
$H_2O + Al^{3+} = AlOH_2^+ + H^+$	-4.96	49.80
$2H_2O + 2Al^{3+} = Al_2(OH)_2^{4+} + 2H^+$	-7.69	Not Available
$4H_2O + 3Al^{3+} = Al_3(OH)_4^{5+} + 4H^+$	-13.88	Not Available
$28H_2O + 13Al^{3+} = Al_{13}O_4(OH)_{24}^{7+} + 32H^+$	-98.73	Not Available
$Na^+ + H_2O = NaOH + H^+$	-14.79	53.65
$SiO_2 + Na^+ + H_2O = NaHSiO_3 + H^+$	-8.30	11.65
$2H_2O + Na^+ + Al^{3+} = NaAlO_2 + 4H^+$	-23.63	190.33
$2H_2O + SiO_2 = H_2SiO_4^{2-} + 2H^+$	-22.96	Not Available
$SiO_2 + H_2O = HSiO_3^- + H^+$	-9.95	25.99
$8H_2O + 4SiO_2 = H_4(H_2SiO_4)_4^{4-} + 4H^+$	-35.94	Not Available
$8H_2O + 4SiO_2 = H_4(H_2SiO_4)_4^{2-} + 2H^+$	-13.64	Not Available

Table S2: Ionic strength, pH, and aqueous species activities for crystalline N-A-S-H

Bulk Si/Al Ratio	Replicate (No.)	Ionic Strength (mol/kgw)	pH	{H ⁺ } (mol/kg soln.)	{OH ⁻ } (mol/kg soln.)	{H ₄ SiO ₄ ⁰ } (mol/kg soln.)	{H ₃ SiO ₄ ⁻ } (mol/kg soln.)	{H ₂ SiO ₄ ⁻² } (mol/kg soln.)	{AlO ₂ ⁻ } (mol/kg soln.)	{Al ³⁺ } (mol/kg soln.)	{Na ⁺ } (mol/kg soln.)	logK
1	1	9.58E-01	13.07	8.27E-14	5.77E-01	1.53E-07	4.42E-04	2.18E-04	4.27E-03	6.57E-35	6.07E-01	11.20
1	2	9.75E-01	13.08	8.12E-14	5.87E-01	1.39E-07	4.10E-04	2.06E-04	4.70E-03	6.74E-35	6.18E-01	11.18
1	3	9.54E-01	13.07	8.30E-14	5.75E-01	1.47E-07	4.25E-04	2.09E-04	4.35E-03	6.78E-35	6.05E-01	11.16
1.5	1	9.39E-01	13.06	8.51E-14	5.61E-01	5.09E-07	1.43E-03	6.88E-04	1.38E-03	2.37E-35	5.93E-01	11.03
1.5	2	9.42E-01	13.06	8.48E-14	5.63E-01	5.10E-07	1.44E-03	6.93E-04	1.40E-03	2.38E-35	5.95E-01	11.11
2	1	8.99E-01	13.04	8.96E-14	5.34E-01	7.83E-07	2.10E-03	9.58E-04	1.05E-03	2.22E-35	5.68E-01	10.90
2	2	9.38E-01	13.06	8.57E-14	5.57E-01	7.19E-07	2.01E-03	9.57E-04	7.85E-04	1.39E-35	5.91E-01	10.84
2	3	9.34E-01	13.05	8.61E-14	5.54E-01	7.47E-07	2.07E-03	9.84E-04	1.05E-03	1.91E-35	5.89E-01	11.12

Table S3: Ionic strength, pH, and aqueous species activities for amorphous N-A-S-H

Bulk Si/Al Ratio	Replicate (No.)	Ionic Strength (mol/kgw)	pH	{H ⁺ } (mol/kg soln.)	{OH ⁻ } (mol/kg soln.)	{H ₄ SiO ₄ ⁰ } (mol/kg soln.)	{H ₃ SiO ₄ ⁻ } (mol/kg soln.)	{H ₂ SiO ₄ ⁻² } (mol/kg soln.)	{AlO ₂ ⁻ } (mol/kg soln.)	{Al ³⁺ } (mol/kg soln.)	{Na ⁺ } (mol/kg soln.)	logK
1	1	9.21E-01	13.05	8.66E-14	5.50E-01	4.61E-07	1.27E-03	2.38E-02	1.66E-02	3.07E-34	5.96E-01	12.24
1	2	9.21E-01	13.05	8.65E-14	5.51E-01	4.56E-07	1.26E-03	2.36E-02	1.63E-02	3.00E-34	5.96E-01	12.03
1.5	1	9.12E-01	13.05	8.74E-14	5.45E-01	7.48E-07	2.05E-03	3.78E-02	1.01E-02	1.94E-34	5.89E-01	12.01
1.5	2	9.12E-01	13.05	8.73E-14	5.46E-01	7.41E-07	2.03E-03	3.75E-02	9.89E-03	1.89E-34	5.89E-01	12.21
2	1	9.06E-01	13.04	8.82E-14	5.40E-01	9.47E-07	2.57E-03	4.71E-02	8.14E-03	1.63E-34	5.84E-01	11.94
2	2	9.05E-01	13.04	8.83E-14	5.39E-01	9.61E-07	2.60E-03	4.77E-02	8.04E-03	1.61E-34	5.83E-01	12.14